Journal of Electroanalytical Chemistry 944 (2023) 117627

Contents lists available at ScienceDirect

Journal of Electroanalytical Chemistry

journal homepage: www.elsevier.com/locate/jelechem

Incremental capacity analysis (dQ/dV) as a tool for analysing the effect of ambient temperature and mechanical clamping on degradation

Lena Spitthoff [a], Preben J.S. Vie [a,b], Markus Solberg Wahl [a], Julia Wind [b], Odne Stokke Burheim [a,*]

[a] Department of Energy and Process Engineering, Norwegian University of Science and Technology (NTNU), Trondheim 7491, Norway
[b] Institute for Energy Technology, NO-2027 Kjeller, Norway

ARTICLE INFO

Keyword:
Lithium-ion Batteries
Incremental Capacity Analysis
Degradation
Commercial pouch cell
NMC

ABSTRACT

This work presents a comprehensive degradation study of two types of large lithium-ion pouch cells; 26 NMC532/Graphite (64 Ah) and 9 NMC433/Graphite (31 Ah) pouch cells. The cells were degraded under different cycling conditions and periodically characterized at room temperature. Specifically, the effect of different ambient temperatures and constraining the cells by clamping was studied. Incremental capacity analysis is an *in situ*, non-invasive characterization technique that allows the identification of battery degradation modes, and is a technique that does not require additional and advanced equipment. Therefore, in this study we also look into applying the analysis technique on an existing data set. This is done by combining incremental capacity analysis on a qualitative level with the tracking of features of interest in the incremental capacity curve as a function of State of Health and utilizing the simulation of different degradation modes for a more in-depth analysis. We combine simulation and experimental incremental capacity analysis with conclusions from capacity loss and resistance changes with a focus on understanding the benefit and limitations of the incremental capacity analysis for large cells. This is important, as incremental capacity analysis is a relatively fast analysis to qualify large commercial batteries for 2nd life applications. Specifically in this study, we found that degradation and capacity loss do not always correlate. For the *64 Ah Cells* cycled at 15 °C and 25 °C, the rate of capacity loss appeared to be similar, although the degradation modes and mechanisms are found to be very different. The clamping was the most important factor for impeding degradation. The *31 Ah Cell* cycled at low temperatures showed a very poor cycling performance, where the incremental capacity analysis revealed that Loss of Lithium Inventory from fast and irreversible plating was responsible.

1. Introduction

In the transition from flexible fossil fuel-based energy to intermittent renewable energy sources, reliable energy storage technologies become indispensable for the future energy economy [1]. Lithium-ion batteries (LIB) represent one of few large scale energy storage technologies, with possibility for distributed and centralised storage systems, as well as both mobile and stationary applications. An inevitable and everlasting challenge to overcome, is improving and understanding the life time prospect of LIBs. Increasing the lifetime of LIBs is therefore an important parameter to consider due to the limitations of resources and the global warming impact [2].

The deterioration of performance over time is observed both as a reduction in the available energy and in the available power. This results from capacity loss and a resistance increase due to degradation, which may be caused by different mechanisms. However, all degradation does not necessarily lead to a loss of capacity and resistance increase. Degradation is frequently studied for different cell chemistries. Battery degradation is known to be a result of several simultaneously occurring physico-chemical processes, leading to Loss of Li

Abbreviations: BOL, Beginning of life; DM, Degradation Mechanism; dQ/dV, Change in capacity with change in voltage; dQ_N/dV, Change in capacity with change in voltage, normalized by initial capacity; DV, Differential Voltage; DVA, Differential Voltage Analysis; EOL, End of life; EV, Electrical vehicle; F1, F2, F3, Feature 1, Feature 2, Feature 3; FEC, Fully equivalent cycle; FOI, Feature of Interest; HPPC, High power pulse test; IC, Incremental Capacity; ICA, Incremental Capacity Analysis; LAM, Loss of active materials; LAMdePE, Loss of delithiated positive electrode active material; LAMdeNE, Loss of delithiated negative electrode active material; LIB, Lithium ion battery; LLI, Loss of Li inventory; NE, Negative electrode; NMC, Lithium nickel cobalt manganese oxide; OCV, Open Circuit Voltage; ORIPE, Ohmic resistance increase at the positive electrode; ORINE, Ohmic resistance increase at the negative electrode; PE, Positive electrode; p-OCV, pseudo-OCV; SEI, Solid electrolyte interphase; SOC, State of charge; SOH, State of health.

* Corresponding author.
E-mail address: Odne.S.Burheim@ntnu.no (O.S. Burheim).

https://doi.org/10.1016/j.jelechem.2023.117627
Received 5 May 2023; Received in revised form 18 June 2023; Accepted 20 June 2023
Available online 30 June 2023

Inventory (LLI), Loss of Active Materials (LAM), and impedance increase due to reaction kinetics degradation [3]. These degradation modes (DMs) refer to the impact of the degradation on the voltage response, rather than the actual mechanisms of degradation. LLI is mainly caused by the growth and decomposition of the solid electrolyte interface (SEI) layer, electrolyte decomposition, Li plating and dendrite formation. LAM can occur only on either or both electrodes at the same time. It can arise from the dissolution of material, structural degradation, particle isolation, corrosion of the current collector, loss of electric contact and electrode delamination. Increased resistance is a result of the formation of passivating films at the active particle surfaces, pore-clogging, as well as electrolyte conductivity losses and loss of electric contact [4]. The increase in internal resistance causes an earlier termination of the charging or discharging process, effectively limiting the available capacity, especially at higher current rates. Degradation is influenced by time, (ambient) temperature, current load, voltage, accumulated ampere-hour throughput, and mechanical stress [4–8]. Several techniques are commonly applied and reported within the literature to identify and quantify the effects of degradation and the different degradation modes (e.g., LLI, LAM, resistance increase). These are often classified into *in situ* and *ex-situ* electrochemical techniques. Incremental Capacity Analysis (ICA) and Differential Voltage Analysis (DVA) are in situ electrochemical methods that are non-invasive characterisation techniques [9]. Both ICA and DVA are methods used to identify and quantify changes in the electrochemical properties of the cell, based on voltage measurements under constant current charge or discharge. While DVA is defined as the rate of change in voltage with a change in capacity (dV/dQ), ICA is defined as the rate of change in charge with a change in voltage (dQ/dV). From a literate explanation this can initially appear somewhat complex. [10].

Graphically the relation between a classic voltage-capacity plot and a (dQ/dV)-voltage plot is examplified in Fig. 1 by presenting the two plots next to each other. The plateaus in the voltage become peaks in the Incremental Capacity (IC) curves (shaded blue), whereas steep increases in the voltage between two plateaus are seen as local minima (shaded green). For half cells, the incremental capacity (IC) peaks correspond to phase transitions in the active electrode material due to intercalation and deintercalation of lithium [11]. The IC curve of a full cell is the convolution of the IC curves of both half cells and the attribution of the peaks are more complex [12].

IC curves have frequently been used to analyse SOH of LIB. This goes from using the intensity of peaks to estimate the SOH [13–18] to more thorough analysis of the IC signatures to help with the differentiation of different degradation mechanisms [3,19,20] or using it as a tool to predict battery cycle life [21]. This is often done by combining ICA with other experimental measurement techniques like electrochemical impedance spectroscopy [20], alternating current impedance [15], differential pressure analysis [22], or utilizing the rate dependency of the ICA [23]. Another approach is coupling the experimental results with modelling [13,10], machine learning tools [21,24] and more advanced analysis methods, like grey relational analysis in combination with the entropy weight method [25], or gaussian process regression [14]. In addition, ICA and DVA methods have been developed for onboard battery SOC and SOH estimation [26–28].

In order to obtain high-quality ICA curves, the measured potential should be close to the open circuit voltage (OCV). Currents in the range of C/10 or lower are recommended, ensuring that the total overpotential is close to zero and thus negligible. To minimize excessive measurement time while at the same time maintaining sufficient quality, work has been done to correct for the effect of overpotentials at higher currents (C/6) [29]. This was done by calculations of the resistance from the voltage change during short interruptions in the current.

ICA can be used on both full-cell and half-cell data. ICA on half cell level allows the attribution of specific features to either the positive or negative electrode, although the convolution of the two half-cells is not straight forward [12]. Each electro-active material will go through its own unique set of structural changes through intercalation/deintercalation and therefore has a unique voltage signature.

In this paper, we present an experimental degradation study of two different commercial LIB pouch cells; a 64 Ah NMC532/Graphite cell and a 31 Ah NMC433/Graphite cell – focusing on the effect of different temperatures and mechanical clamping. We utilize ICA to study the effects of these external impact factors on the degradation pathways, using a 5-step procedure presented in Section 2. Section 3 then presents the set-up and extent of the experimental degradation study, and Section 4 presents the results and discussion following the 5-step analysis procedure. The novelty of this work is tracking the features-of-interest (FOI) for a large experimental data set across a wide range of ambient temperatures during cycling and combining this with tracking the FOI of IC curves simulated for different degradation modes based on half cell data.

2. Methodology: Incremental Capacity Analysis (ICA)

In this study, ICA was utilized to study the effects of external impact factors on the degradation pathways. This section will first present the IC signature of the commercial 64 Ah NMC532/Graphite cell and how it is convoluted from the separate electrode IC signatures to aid a better understanding of the further analysis (Section 2.1). The main part of this section introduces the 5-step procedure used for analysis in more detail. It is schematically presented in Fig. 2.

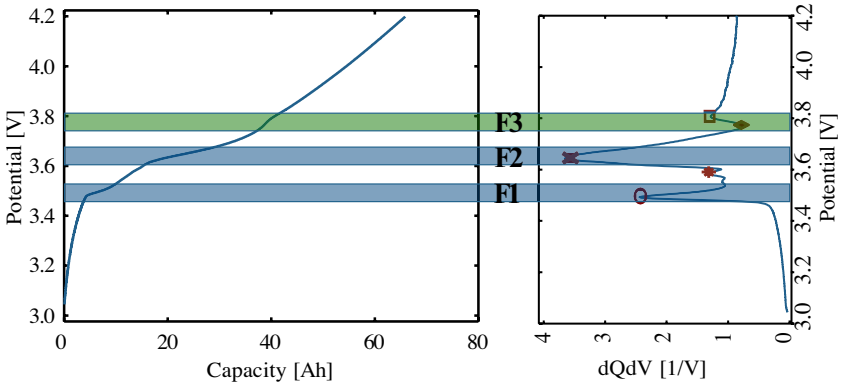

Fig. 1. Charge potential vs capacity (left), normalized dQ/dV vs. potential (right).

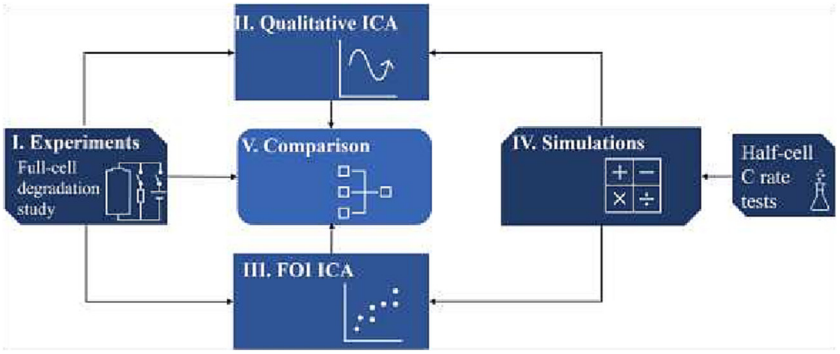

Fig. 2. 5-step procedure used for degradation analysis in this study.

(I) Determining capacity loss and changes in resistance.
(II) ICA: Qualitative description and initial evaluation e.g. identifying FOI, allocation of peaks using half cell data (Section 2.2).
(III) ICA: Tracking FOI and comparing the effect of different operation conditions on the development of those features (Section 2.3).
(IV) ICA: Simulation of different degradation modes using the alawa toolbox to obtain degradation maps for the cell under investigation (Section 2.4).
  (i) Qualitative comparison.
  (ii) Using the same method of tracking FOI as for the experimental data.
(V) Comparing experimental and simulation results for further analysis.It has to be noted that when describing the IC curves on a qualitative level (steps II and IVi), we acknowledge that the correct voltage of the peak for ICA is the onset of the peak as this is the potential at which the reaction starts. However, for feasibility and reproducibility, we use the potential that corresponds to the peak maximum and not the front of the peak when tracking FOI (steps III, IVii). This appears to be a fair compromise for our data set as the observations from both methods are in agreement (compare Fig. 6).

As the original voltage versus capacity curves contain measurement noise, it is necessary to apply a filtering algorithm to obtain the IC data. Since the number of data points per capacity step might be uneven, the measured voltages are averaged in capacity steps of 0.05% of the full capacity span. After averaging the dataset, a local second order polynomial regression was fitted to the voltage as a function of capacity with a moving capacity window. The size of the moving capacity window is limited by either a voltage window (20 mV) or capacity window (5%) whichever being the limiting variable.

2.1. IC signature - a general description

Fig. 3 presents the IC curves of the NMC532 positive electrode (A) and graphite negative electrode (B) and the full cell (C) of the 64 Ah NMC532/Graphite cell used in the degradation study. The negative electrode and positive electrode potentials are measured versus Li metal. The main reactions are numbered from high to low for the NMC positive electrode and from low to high voltage for the graphite negative electrode, in accordance with Dubarry et al.[12]. The numbering is reversed for the negative electrode as it is going through the opposite process (lithiation/delithiation) to that of the positive electrode. Starting with the positive electrode (Fig. 3A), the response is mainly made of a broad shoulder at high voltage (1) and a well-defined, broader peak at low voltage (2). The graphite negative electrode (Fig. 3B) is made of three well-marked peaks (1, 2, 5) and two small peaks (3,4) with peak (4) being barely visible. Fig. 3 C presents the complex response of the full cell including the graphite negative

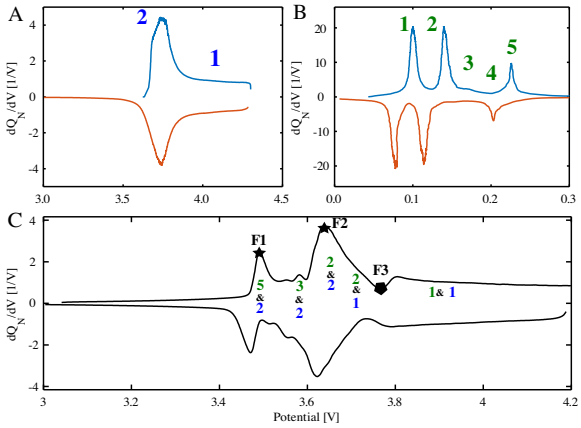

Fig. 3. C/20 electrochemical behaviour for the NMC532 positive electrode (A) and graphite negative electrode (B) and the full 64 Ah NMC532/Graphite cell (C).

electrode and NMC positive electrode from Fig. 3 A and B. The electrode peaks are convoluted to peaks in the full cell, marked in Fig. 3 C. A thorough explanation using a clepsydra analogy is done by Dubarry et al. [12]. In summary, they suggest imagining the IC curve of each half-cell as being the shape of each bulb of a clepsydra (hourglass). Considering the charge, at beginning of the charge the positive electrode is nearly full and the negative electrode empty. The negative electrode is then filled, starting with the highest voltage peak (5) and moving to lower voltages. The positive electrode is simultaneously emptied, moving from low (2) to high potentials. The potential of the full curve corresponds to the potential difference of the reactions in each electrode.

2.2. IC signature and degradation analysis (Step II.)

When analysing IC curves, the balancing of the electrodes becomes important – and with this the loading ratio (LR). LR is commonly defined as the ratio of the capacity of the negative electrode to the capacity of the positive electrode. Cells are usually designed in a way that the LR is larger than one, i.e., with a larger negative electrode capacity [12]. For most commercial electrodes the electrochemical behaviour of the electrodes does not change significantly but rather the degradation affects the electrode balance.

Ohmic resistance increase (ORI) alters the potential of both electrodes with the amount of ORI, without changing the LR or the SOC offset. It manifests as a shift of the IC signature towards higher voltages during charge and a shift towards lower voltages during discharge, without changing the height of the peaks. The potential shift due to

ORI is in the range of the cell resistance times the current used for the IC curve (e.g. C/20 or C/10 in our studies).

The impedance of the cell can also increase due to a Faradaic rate degradation, causing the kinetics of one of the half-cell reactions to change. This leads to an IC peak broadening as the voltage plateau shortens. The voltage plateau shortening is caused by a slowing down of the kinetics (e.g the disparity in the extent of reaction throughout the electrode increases with degradation) resulting in a more gradual change in voltage, and an increase in charge transfer resistance.

LLI occurs when Li ions are consumed by parasitic reactions. This results in a reduction of cyclable Li ions in the system. The lack of cyclable Li ions becomes noticeable in the IC curve at the end of charge and discharge as the amount of Li ions remaining is insufficient to fully fill up the negative electrode and positive electrode respectively. Usually, the main cause of LLI is the growth of SEI on the negative electrode but it can also occur when growing a passivation layer on the positive electrode or due to irreversible Li plating.

LAM affects the LR. If LAM occurs at the positive electrode (LAMdePE), the LR increases, while it decreases in the case of LAM at the negative electrode (LAMdeNE). LAM also changes the current density at the affected electrode as both the active surface area and the material that can accept charge are reduced. With LAMdeNE, the risk for Li plating increases, especially if the LR decreases below 1 because the negative electrode will be fully lithiated before the positive electrode completely releases all Li ions. [3].

2.3. Feature analysis (Step III.)

Regarding the analysis of IC and differential voltage (DV) curves, Dubarry et al. [16,30] suggested the use of FOIs. Suggested FOIs are back tail, peak slope, peak/arch intensity and voltage, intensity difference between peaks, the voltage difference between peaks, peak/arch half-width, and front tail. By simulating all possible degradation paths using the *'Alawa toolbox* developed by Dubarry et al. [3], a look-up table can be compiled which can be used for onboard diagnosis using the FOIs. Dubarry et al. [3] employ the developed method using data from earlier small-scale degradation studies on commercial pouch LTO/NMC cells operated at 25 °C and with C/3 charge and discharge current, and cylindrical commercial 2.3 Ah graphite/LFP cells operated at 23 °C and a variation of operation conditions. They report to be able to diagnose about 90 % of the degraded cells successfully.

Dubarry et al. [31] showed using a synthetic data set, that FOI based diagnosis can offer accuracies below 1 % up to 400 cycle for LLI, LAM and SOH estimations when several FOIs are considered together.

Stroe et al. [18] investigated changes in certain FOIs due to degradation from calendar-ageing 63 Ah LMO/NMC vs. graphite cells. They compare the FOIs on cell and module levels, to evaluate the suitability of the different features as a SOH estimator for EV applications. The most suitable FOIs for SOH estimation are identified, but a direct relationship between those features and the SOH is not established. Zheng et al. [10] used three different FOIs to estimate both SOC and SOH. They reported a maximum absolute error of 1.0 % and a relative error of 2.0 % for battery SOC and SOH estimation, respectively. This study is based on three 60 Ah LFP/graphite cells that have been charged and discharged with 0.5 C at room temperature.

For NMC532/graphite cells and NMC111/graphite cells Dubarry et al.[12] suggest to use the intensity of the shoulder at high voltage, the intensity and position of the minimum around 3.8 V and the intensity and position of the maximum intensity for peaks around 3.45 V and 3.7 V.

2.4. Simulation (Step IV.)

To support the discussion around the underlying degradation mechanisms we use the *'Alawa* toolbox by Dubarry et al. [3]. This is a widely used tool based on a mechanistic model composed of two layers: a top layer with cell configuration and inputs from cell operating and degradation modes and a sub-layer with half-cell modules that describe the electrode behaviour. The simulation in this work was performed using half-cell data from the 64 Ah NMC532/graphite cell.

3. Experimental

In this paper degradation data from two cycle-life studies was examined and studied to further understand the degradation mechanisms involved. The two studies involved cyclic degradation of large LIB pouch cells at different operation conditions. The largest LIB was a NMC532/graphite cell with a nominal capacity of 64 Ah. The second cell was the XALT 31 HE NMC433/graphite cell with a nominal capacity of 31 Ah. For simplification, we will refer to the NMC532/graphite cell with a nominal capacity of 64 Ah as the *64 Ah Cell* and the Xalt 31 HE cell as the *31 Ah Cell* in the remainder of this paper. The *64 Ah Cell* was operated between the lower voltage limit of 3 V and an upper limit of 4.2 V, while the *31 Ah Cell* was operated between 2.7 V and 4.2 V, according to the manufacturers' specifications.

3.1. Degradation study

All cells were characterized at an ambient temperature of 25±1 °C. The characterization included a 1 C cycle, a low C-rate cycle (C/20 for *64 Ah Cell*, C/10 for *31 Ah Cell*) and a high power pulse characterization test (HPPC) to obtain the ohmic resistance in the cell. The characterisation routine was performed periodically with intervals of 100–200 cycles or for every 5 %-point loss in SOH.

The cycle-life study was set up as an accelerated study to obtain battery-life data within a reasonable time. Charge and discharge currents were selected based on the maximum rates advised by the battery cell manufacturer.

Since the battery temperature is a well-known factor that affects battery life [32], the cells were cycled at ambient temperatures in the range of 5 to 45 °C. All cells were cycled in the full SOC window. The charge was performed as constant current constant voltage while the discharge was only constant current. In addition, the *64 Ah Cell* was cycled both with and without being mechanically clamped. This was obtained by fixing the pouch cells between two 1 cm thick aluminium plates and secured with bolts (Fig. 4). Each bolt was fixed with 1 Nm torque.

The full cycle life test matrix is presented in Table 1.

Table 2 shows the number of cells cycled with identical conditions, in order to study the effect of the ambient temperature. All *64 Ah Cells* are cycled clamped and with a C-rate of 0.75 (total 14 cells). All *31 Ah Cells* are cycled with a C rate of 1 and without clamping (in total 9 cells). When investigating the effect of clamping we analyse the behaviour of 19 cells that have been cycled with applied MP (0.4 C, 0.75 C and 1.5 C) and 7 cells that have been cycled without clamping. All cells are cycled in the full state of the charge window.

Fig. 4. The clamping set-up used in this study.

Table 1
Test conditions during cycle life studies and characterization tests.

General info		
	64 Ah Cell	31 Ah Cell
Capacity [Ah]	64	31
positive electrode	NMC532	NMC433
Cycle life study		
Amount of Cells	25	8
Temperature [°C]	5, 15, 25, 35, 45	5, 25, 45
C rate	0.4, 0.75, 1.5	1
SOC window [%]	0–100	0–100
MP [NM]	0/ 1 on bolt (Fig. 4)	0
Characterization		
Temperature [°C]	25	25
HPPC	0.75 C	1 C
High C rate	0.75 C	1 C
Low C rate	C/20	C/10

Table 2
Amount of cells cycled under the same condition - studying the effect of ambient temperature. All *64 Ah Cells* are cycled clamped and with a C rate of 0.75. All *31 Ah Cells* are cycled with a C rate of 1 and no clamping.

Temperature [°C]	64 Ah Cell	31 Ah Cell
5	3	2
15	1	-
25	6	4
35	2	-
45	2	3

3.2. Incremental Degradation Measurements

Full cell. Characterization tests were conducted at an ambient temperature of 25°C inside a ventilated temperature chamber. The characterization included a slow discharge and charge cycle for ICA. For the *64 Ah Cell* a current of C/20 was used and for the *31 Ah Cell* a current of C/10.

Half cell. One *64 Ah Cell* was disassembled at beginning of life (BOL). Both negative electrode and positive electrode were washed in DMC (dimethyl carbonate). One side of the electrode coating was removed and discs with an area of 1.767 cm^2 were cut out, which were assembled in coin cells with Li metal as the counter electrode. The following cycling protocol was used: C/20 (2 cycles), C/10 (3 cycle), C/5 (3 cycle), C/2 (1 cycle), 1 C (3 cycle), 2 C (3 cycle), C/20 (3 cycle).

3.3. Features of Interest (FOI)

We track three features as functions of SOH. These features are marked as an example for the IC signature at BOL in Fig. 1 and Fig. 3. Specifically, it is the intensity and voltage of the peaks around 3.49 V, 3.64 V and the minimum at 3.77 V (potentials at BOL). Those features are in agreement with what has been suggested in literature for this chemistry (Section 2.3). In contrary to what is suggested in literature, the intensity of the shoulder at high voltage is not tracked as it is difficult to distinguish and track reliably for the degraded cells in this study. They will be referred to as Feature 1 (F1, peak at 3.49 V), Feature 2 (F2, peak at 3.64 V) and Feature 3 (F3, minimum at 3.77 V), marked in blue and green.

The FOIs were tracked by extracting the value and location of the local maxima of the normalized differential change in charge with change in potential (dQ_N/dV) versus potential in the region of interest (grey in Fig. 1). The dQ/dV was normalized to the initial capacity of the cell to allow comparison of the different cell types. The shift in voltage was calculated from the actual potential of the maxima minus the potential of the respective maxima at BOL. Together with the height of the peaks, these features were examined both separately and in comparison, in order to analyse the effect of different cycling conditions.

3.4. Simulation

The half-cell data was experimentally obtained by extracting the electrodes from the *64 Ah Cell* at BOL and cycling them with Li metal as the counter electrode as described in Section 3.2. The half-cell data was used to simulate the potential and IC curve at C/20 which allowed to simulate the effect of the degradation modes. Both the loading ratio (LR) and SEI offset were estimated by comparing the simulated IC curve of the full cell at BOL, based on the half-cell data, to the experimentally obtained IC curves of the *64 Ah cell* at BOL. This resulted in an LR of 1.1 and an SEI offset of 2 % which is well within what is reported for LIBs using layered transition oxide positive electrodes and graphite negative electrodes[12]. The changes in the IC curve with degradation were then simulated by isolating single DMs. The analysis focused on ORI, LAM and LLI. For LAM it is differentiated if there is a loss in the negative electrode (NE) or positive electrode (PE). We assume a degradation of 0.01 % per cycle and a resistance increase of 1 % per cycle, simulating 2000 cycles. All other parameters are determined by comparing experimental and simulation results at BOL and are kept constant for all simulations. We extract F1, F2 and F3 in the same way as for the experimental data (as explained in Section 3.3).

4. Results and Discussion

In the following, we present the results from the degradation study using the 5-step analysis process presented earlier. We explain the process in detail for the *64 Ah Cell* when examining the effect of ambient temperature. To demonstrate the applicability to other cell types, we use the same process when analysing the effect of clamping on the same cell and the effect of temperature on the *31 Ah Cell*.

4.1. 64 Ah cell: Effect of Temperature

The cells analysed in this section are the *64 Ah Cell*, which were cycled in the full SOC window. The charge and discharge current used for cycling was 0.75 C. All cells were mechanically clamped. All cell behaviour (*64 Ah Cell*) presented and discussed in the course of this paper are presented but only the cells focused on in this section are coloured while the remaining cells are depicted in grey in the figures (e.g. Figs. 5, 7 11, 12). The intention is to help the reader obtain a full picture of the different operating conditions, to enable comparisons. The cells marked in grey will be addressed in Section 4.2.

4.1.1. Step I. Capacity Loss and Resistance

Fig. 5 shows the SOH (C/20 capacity normalized by the initial C/20 capacity) versus full equivalent cycles (FEC) (Fig. 5 and the resistance as a function of SOH (Fig. 5b) for the *64 Ah Cell*. The best capacity retention is observed when the temperature of the temperature chamber was around room temperature (15°C (light blue) and 25°C (green)). The capacity loss is accelerated both when increasing and decreasing the temperature, which is well in agreement with what has been reported numerous times in literature [33,32]. The acceleration effect appears to be larger for higher temperatures than for colder temperatures. Cells with the best capacity retention show the largest increase in resistance at the same SOH. Cells cycled at an ambient temperature of 15°C and higher, show an initial decrease in the internal resistance, but the resistances start increasing again as the capacity

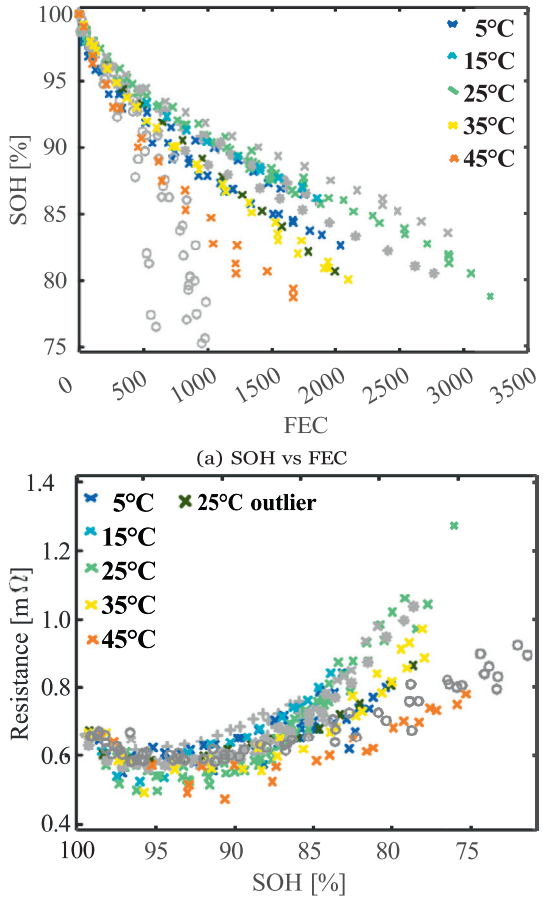

Fig. 5. SOH versus FEC and DC resistance for the *64 Ah Cell* for different ambient temperatures, 0.75 C charging and discharging rate, MC applied. Data in grey are analysed and presented later.

is further reduced. The cells cycled at 5°C (dark blue) never show a decrease in resistance but only an initial constant resistance (until approx. 97 % SOH) before increasing. The dark green data points represent an outlier of the cells cycled at ambient temperatures of 25°C. For this specific cell, the clamping had to be replaced after around 300 FEC. The cell showed a significantly faster loss in SOH and a slower resistance increase, comparable to the cells cycled at an ambient temperature of 35°C.

4.1.2. Step II. Qualitative ICA

We compare the Incremental Capacity (IC) curves at distinct SOH (95±1 %, 90±1 %, 85±1 %) and compare changes in intensity and potential of the defined FOI to those of the BOL curve. Fig. 6 presents the IC curve during charge for the cells cycled at different ambient temperatures, plotted in the voltage window 3.4 V to 3.95 V. The full IC curves of the full voltage window during both charge and discharge are included in the *Supplementary Material*. The line in black represents the IC signature at BOL, the colours represent the cycled cells at the specified SOH - from left to right: 95±1 % SOH, 90±1 % SOH, 85±1 % SOH. Fig. 6 illustrates that both the voltage of the peak onset and the peak voltage correlate. As already mentioned earlier for feasibility and reproducibility, we use the potential that corresponds to the peak maximum and not the front of the peak when tracking FOI although the onset of the peak as this is the potential at which the reaction starts. The changes in the FOIs are summarized using arrows in the tables below the plots. The colour coding in the background of the arrows is intended to guide the reader's view to the most interesting changes. It uses a traffic light system: red is negative, green positive and orange is constant. The colour in the background of the temperatures refers to the change in resistance in comparison to the resistance at BOL.

At 95 % SOH (Fig. 6, left), the shift of the minimum at high voltage (F3) to higher voltages and a small decrease in intensity for temperatures of 25°C and higher is most noticeable. The changes in F1 and F2 are less extreme, but we observe a decrease in intensity for both peaks and all conditions. Both peaks shift to higher potentials for ambient temperatures of 15°C and lower, are steady for cells cycled at 25°C and shift to lower potentials for cells cycled at 35°C and higher.

LLI causes a decrease in peak height and a shift towards higher voltages, which for the cells cycled at 35°C and higher, appears to be overlapped resulting in an shift to lower voltages. Calculating the IR drop resulting from the measured resistance decrease makes it apparent that the resistance decrease is not responsible as the voltage drop was by a magnitude smaller than the observed shift. This will be explained in greater detail when comparing the experimental and simulation results in Section 2.4.

At 90 % SOH the minima at high potential (F3), and also the small peak around 3.6 V, becomes less distinct for the cells cycled at 15°C and lower. In addition, for the cells cycled at 25°C and lower,F2

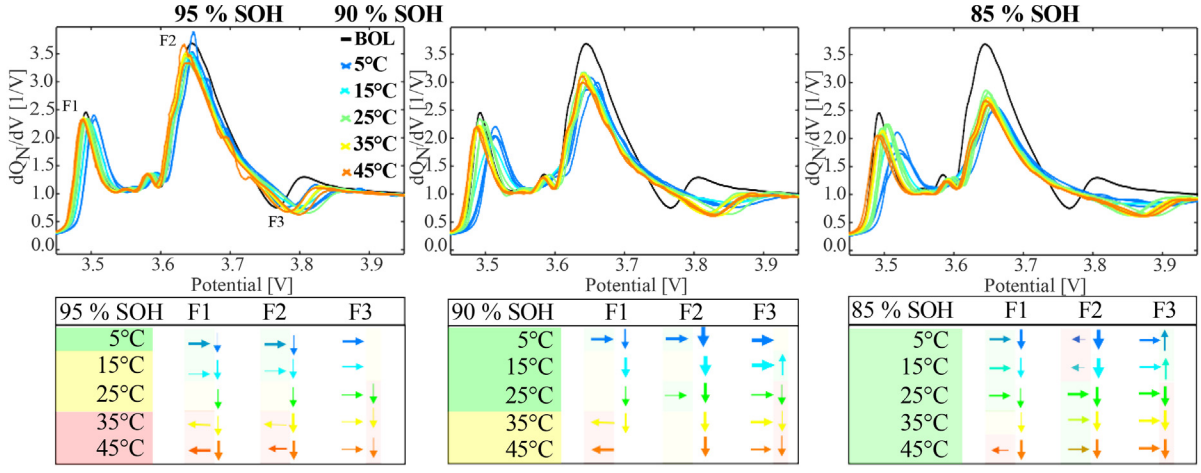

Fig. 6. IC curves at 95±1 % SOH, 90±1 % SOH and 85±1 %SOH for the *64 Ah Cell*, cycled at different ambient temperatures, 0.75 C charging and discharging rate, MP applied. The table summarizes the FOI evolution with degradation. The font size is representative of the intensity of changes.

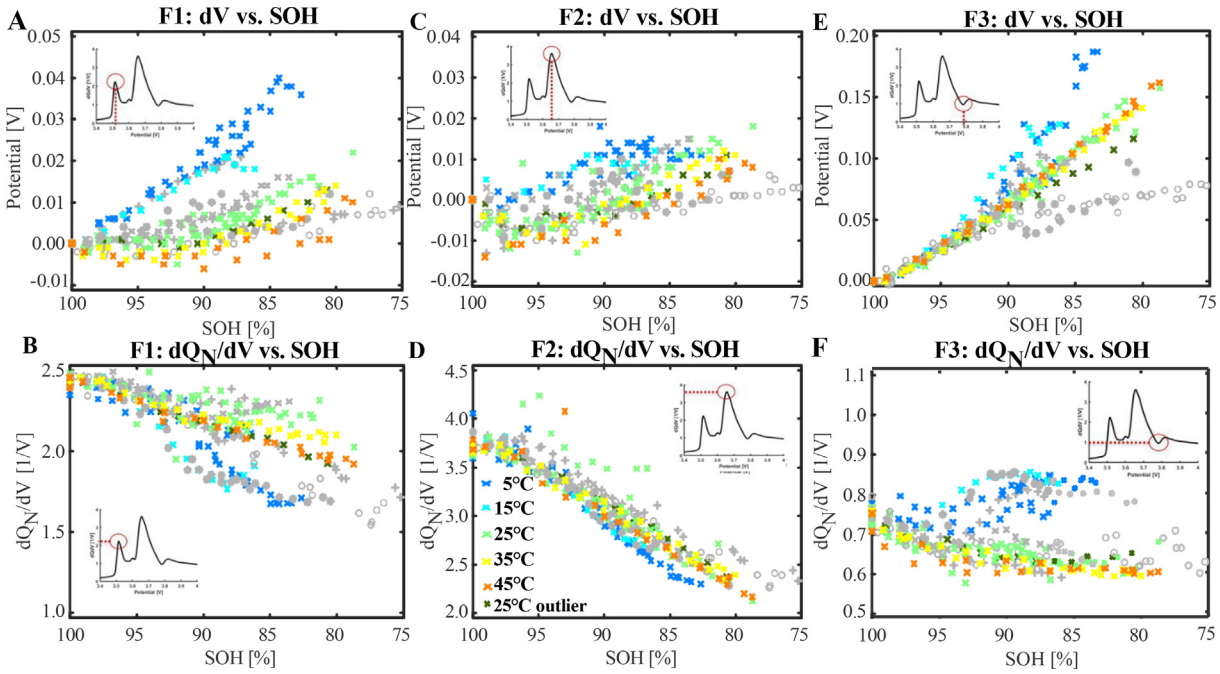

Fig. 7. Potential (A, C, E) and intensity (B, D, F) shift of F1, F2 and F3 versus SOH for the *64 Ah Cell* for different ambient temperatures, 0.75 C charging and discharging rate, and MP applied. The grey-colored data represents cells analyzed later.

appears to reverse its shift and increase back to similar potentials as at BOL. F1 shows a distinct clear shift to higher potentials for low ambient temperatures. This indicates that LLI appears to be still the main degradation mechanism accompanied by an OR decrease at lower temperatures. The shift of F1 to lower potentials compared to BOL for high ambient temperatures is discussed in more detail in Section 4.1.5. At around 90 % SOH, the OR does not show a decrease compared to BOL anymore (Fig. 5b), supporting the observation that the shift was not primarily caused by OR decrease at 95 % SOH either. The disappearance of F3 and the small peak at lower potentials appear to be an indication of inhomogeneities as it compares to the simulated changes in IC curves due to inhomogeneities presented by Dubarry et all. [12].

At 85 % SOH, the same trends as observed for 90 % SOH become more evident. LLI still appeared to be the main degradation mechanism, especially for higher temperatures and inhomogeneity appeared to be more significant for low ambient temperatures.

4.1.3. Step III. Feature ICA

Fig. 7 presents the intensity and potential shift of F1, F2 and F3. We explain the graph in more detail using the example of the cell cycled at 35°C (yellow). The plots of the top row (Fig. 7 A, C, E) present the potential shift of F1, F2 and F3, i.e., the potential of the peak at the specific SOH subtracted by the potential of the peak at BOL. The plots of the bottom row (Fig. 7 B, D, F) present the normalized intensity (dQ_N/dV) of the peak versus the measured SOH. One single data point represents the height of the peak in the normalized dQ/dV (dQ_N/dV) versus voltage plot during C/20 charge as presented in Fig. 1 and 3.

Starting with F1 (Fig. 7 A and B), Fig. 7A presents the potential shift. For example, for 35 °C, we see a negative potential shift for SOH between 100 % SOH and 90 % SOH, referring to a shift of the peak towards lower voltages. The potential shift reaches a minimum at around 93 % SOH before shifting back towards higher voltages. The shift becomes 0 V around 90 % SOH, which means that the dQ_N/dV peak is at the same potential as at BOL. With a further reduction in SOH, the potential shift becomes positive, with the peak is shifting towards voltages higher than at BOL. For 45 °C, the inflexion point in F1 occurs at lower SOH.

The peak height of F1 (Fig. 7 B) is plotted versus the remaining C/20 capacity, normalized by the initial capacity (SOH). The intensity (i.e. height of the peak) starts at around 2.3 V^{-1} and decreases linearly when the capacity reduces to around 2.05 V^{-1}, when the cell reaches a SOH of 80 %.

The potential shift of F1 appears to be clearly dependent on the cycling temperature. When cycling at low temperatures, a linear relationship between potential shift and SOH can be observed. With ambient temperatures of 25 °C and above F1 initially shifts to lower potentials before shifting towards higher potentials. This behaviour becomes more extreme for larger temperatures with the cells cycled at an ambient temperature of 45 °C, returning back to the initial position first at a SOH of around 75 % SOH.

Fig. 7 C and D present the potential shift and the change in intensity for F2 (voltage window 3.65 to 3.75 V), respectively. The potential shift (Fig. 7 C) is negative during the initial capacity loss (e.g peak shifting towards lower voltages) for cells cycled at 25°C and higher, similar to the initial potential shift of F1. The potential shift reaches a minimum at around 95 % SOH and increases upon further loss in capacity. It reaches 0 V around 85 % SOH and with a further reduction in SOH, the potential shift becomes positive, reaching 0.01 V at 80 % SOH. Fig. 7 D presents the normalized intensity of the F2 peak versus the cell SOH. Again, looking at the behaviour of the cell cycled at 35 °C (yellow) first. The intensity (e.g. height of the peak) is around 3.7 V^{-1} at BOL. It stays constant during the initial capacity loss of about 2 % and decreases linearly with a further reduction in capacity. The intensity reduces to around 2.4 V^{-1} when the cell reaches a SOH of 80%.

Looking also at the other temperatures, it becomes noticeable that there is a more clear linear dependency between the intensity of F2 and the SOH than it was observed for F1. In addition, the strong dependency on the ambient temperature during cycling for the potential shift of F1, cannot be observed for F2. Although, below a SOH of approximately 93 % the intensity of F2 appears to be dropping slightly faster for the cells cycled at low temperatures (5 °C and 15 °C).

Fig. 7 E and F present the potential shift and the intensity of F3, the minima in the differential capacity curve within the limits 3.8 to 4 V. There is a clear difference between the cells cycled at low temperature (5 °C and 15 °C) compared to cells cycled at moderate and high temperature (25 °C to 45 °C). Contrary to F1 and F2, the potential shift of F3 is only positive (i.e. shift of the minima to higher potentials). The potential shift initially (until capacity drops to around 92 % SOH) appears to be linear to the SOH for all ambient temperatures. While the dependency stays linear for cells cycled at moderate and high temperatures, it becomes more of an exponential increase for the low-temperature cells.

The intensity of the minima initially drops for all cells when the SOH decreases. The intensity of the minima keeps reducing at a slower rate with further capacity loss for the cell cycled at moderate and high temperatures. The intensity of the minima for cells cycled at low temperatures stays constant with further capacity loss and the minima become not distinguishable anymore for a SOH below approximately 85 % (see Fig. 6). The vanishing of the minima is caused by the more gradual change in potential at high SOC.

In addition, the 25 °C outlier (cell where clamping had to be replaced after 300 FEC) deviates from the linear relationship of the potential shift below a SOH of around 90 % (Fig. 7 E). While the relationship became rather exponential for the low-temperature cells, the slope decreased for the outlier. This deviation is towards the cells cycled unclamped (grey circles in the plot). For the other FOIs (especially the F1 and F2 potential shift and F1 intensity, Fig. 7 A – D) there is also a deviation of the outlier cell from the other cells cycled at an ambient temperature of 25 °C with the effect of clamping appearing. Although these deviations are also towards cells without clamping, it is not as obvious and is similar for cells cycled at higher temperatures.

In summary, distinctly different behaviour was observed for cells cycled at low ambient temperature (15°C and below), although the 15°C cell showed a comparable trend to 25°C when looking at capacity loss and resistance increase. A more drastic drop in intensity and shift towards higher potentials was observed for F1 and F2 for the low-temperature cells, indicating a larger contribution of LLI to the capacity loss. The distinctively different behaviour of F3 might be explained by an increased degree of inhomogeneity for the low-temperature cells. For the cells cycled at 25°C and higher, the potential change of F3 appeared to be proportional to the SOH. F1 and F2 potential shifted to lower voltages before increasing.

4.1.4. Step IV. IC Simulation

IVi. IC Simulation: Qualitative comparison Fig. 8 and 9 present the simulated degradation behaviour for the *64 Ah Cell*. Each degradation mechanism was simulated over 2000 cycles with intervals of 100 cycles. Fig. 9 shows the IC curves each 200 cycle. Looking at the capacity loss (Fig. 8), it is observed that loss of delithiated active material (LAM) is not initially associated with capacity loss both for loss at the negative electrode (LAMdeNE) and positive electrode (LAMdePE). While LAMdePE results in capacity loss after around 300 cycles, LAMdeNE only results in capacity loss after around 500 cycles. Both LLI and Ohmic Resistance Inrease (ORI) result in a linear capacity loss straight away, albeit with different degradation rates. For ORI this is only true when the cell is charged with constant current only. LLI results in a more extreme loss in the capacity even though for the ORI simulation the resistance increase per cycle was already chosen to be simulated as an extreme case.

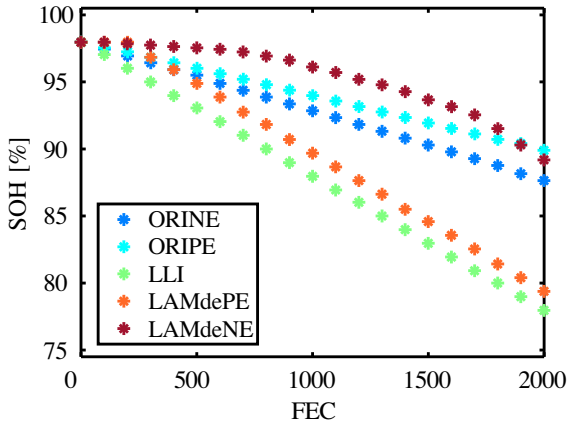

Fig. 8. Simulated SOH versus FEC for the *64 Ah Cell* using *'Alawa* tool. Isolation of single degradation mechanism.

Fig. 9 presents the IC curves for the isolated degradation mechanisms. This is idealistic as in a real application degradation mechanisms and therefore degradation modes are coupled (e.g. LAMdeNE resulting in plating (LLI)) but rather aims to understand how the degradation modes effect the IC curves. LAMdePE (Fig. 9 B) causes F1 to initially shift to lower potentials (until 90 % SOH) accompanied by a drastic decrease in intensity. F2 is shifting to lower potentials and decreasing in intensity. F3 is increasing in intensity and shifting to lower potentials. We recall what we observed for the experimental data in Section 4.1.3: An initial shift of F1 to lower potentials for cells cycled at high temperatures. LLI (Fig. 9 C) results in an F1 shift to higher potentials while increasing slightly in intensity. F2 is shifting to higher potentials together with a significant decrease in intensity, whereas F3 shows a large shift to higher potentials with a small decrease in intensity. From Fig. 8, it can be seen that LLI causes a loss in capacity from the first cycle. The missing Li is resulting in the NE not being filled to the same level at the end of the charge. This is why already at a minimal loss in capacity, the effect of LLI is already very visible for F3, which is the feature at the end of the charge. With a further LLI and therefore capacity loss, it starts to become more visible at F2 as well. ORI (Fig. 9 D) leads to a shift of the full IC curves towards higher voltages, while the intensity remains unchanged.

We recall what was observed for the experimental data in Section 4.1.3: For cells cycled at 35 °C and 45 °C, F3 was decreasing in height and shifting to higher potentials already at 95 % SOH. F2 on the other hand only showed this behaviour at 85 % SOH. This clearly fits well with the LLI mode, where the loss of Li initially only affects the feature at the end of the charge (F3), while additional loss of Li also affects the response at lower voltages during the charge. F1 was initially shifting to lower potentials for cells cycled at 25 °C and higher, was most extreme for high temperatures. Based on the calculated RI drop, ORI was disqualified as the main cause of this observation (see Section 4.1.3). LAMdePE, however, appears to explain this behaviour.

Step IVii. IC Simulation: FOI The last step in the analysis is the FOI analysis using simulation data. Fig. 10 presents the intensity and potential shift of F1, F2 and F3 extracted from the simulated IC curves - similar to Fig. 7 for the experimental data. The plots in the upper panel present the change in the potential of F1, F2 and F3 (A, C, E) compared to the potential at BOL. The plots in the lower panel (B, D, F) present the normalized peak intensities. Again, one single data point represents the height in the normalized dQ/dV (dQ_N/dV) versus voltage plot during C/20 charge.

As expected, ORI results in the same linear shift of the potential for all features while the intensity stays constant. LLI results in a linear increase of the potential shift for all features but the effect is most extreme for F3, followed by F1. In addition, it results in a decrease in intensity for F2 and F3 before it reaches a steady state. F1 shows a slight increase due to LLI.

LAMdePE results in an initial negative potential shift (shift to lower potentials) for all features, but starts to shift back at around 84 % SOH. It results in a more or less constant intensity for all features initially, before it results in an increase for F3, a steady decrease in F2 and a significant decrease in F1.

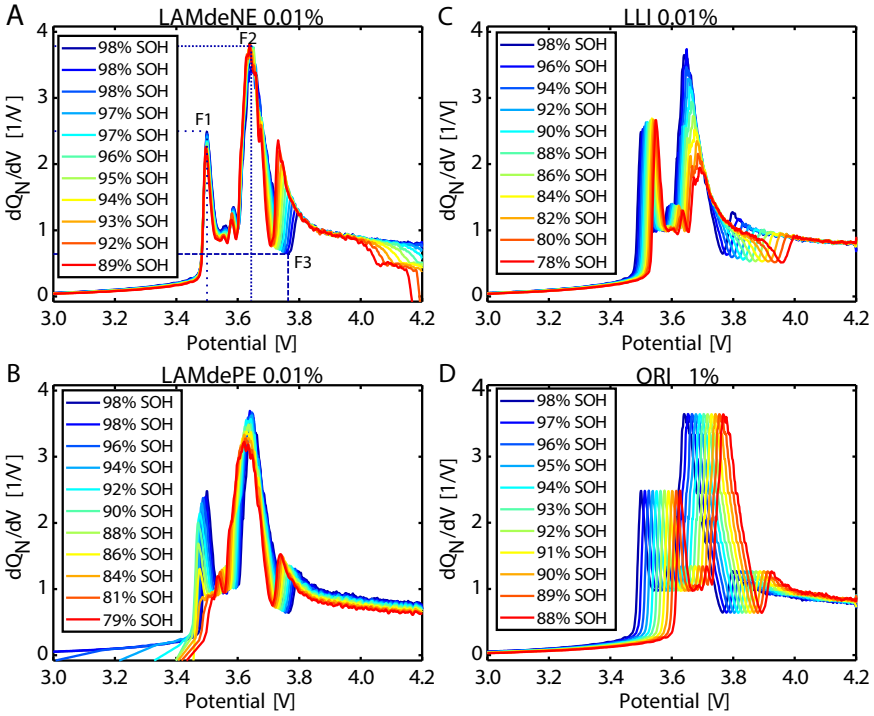

Fig. 9. Degradation map for the *64 Ah Cell* using *'Alawa* tool. Isolation of single degradation mechanism: A) LAMdeNE (Loss of delithiated negative electrode active material), B) LAMdePE (Loss of delithiated positive electrode active material), C) LLI (loss of lithium inventory), D) ORI (Ohmic Resistance Increase).

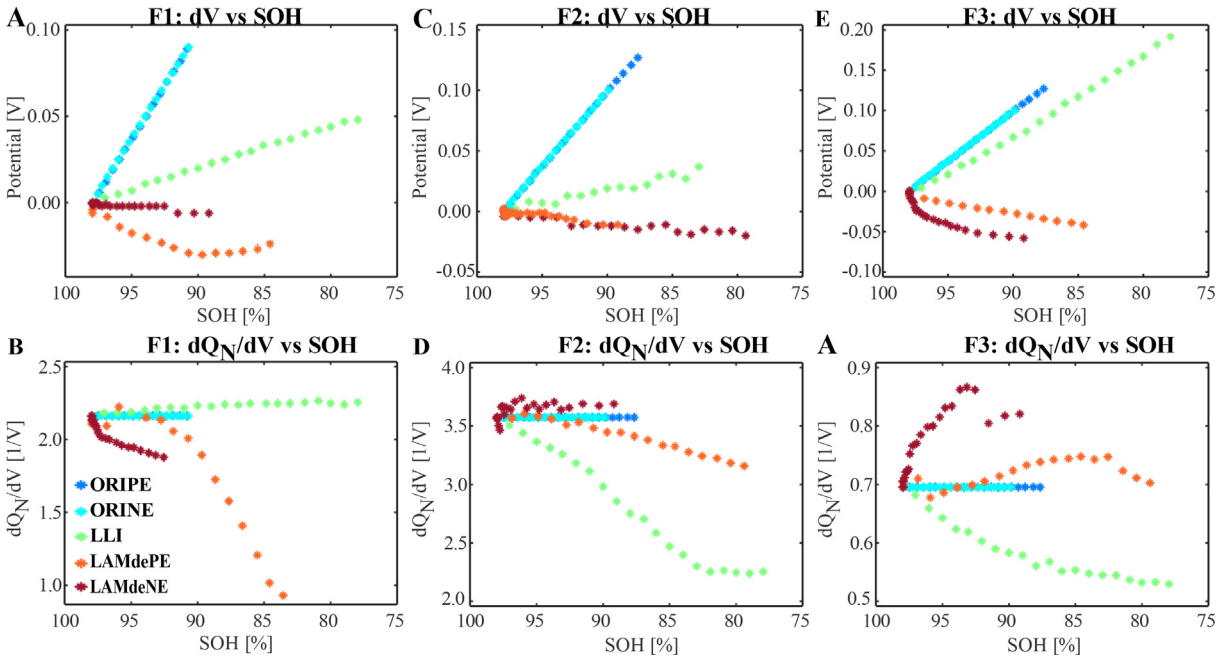

Fig. 10. FOI extracted from simulated degradation maps. Intensity in upper panel (A, C, E), potential change in lower panel (B, D, F). ORINE (Ohmic Resistance Increase at Negative Electrode), ORIPE (Ohmic Resistance Increase at Positive Electrode), LAMdeNE (Loss of delithiated negative electrode active material), LAMLINE (Loss of lithiated negative electrode active material), LLI (loss of lithium inventory). This is idealistic as in a real application degradation mechanisms and therefore degradation modes are coupled.

LAMdeNE also results in a negative potential shift for all features. But while it has a similar effect on F2 as LAMdePE, it results in a more extreme potential shift of F3 and only a very small potential shift of F1. LAMdeNE results in a decrease in the intensity of F1, a more or less constant intensity of F2 and an increase in the intensity of F3.

Comparing this with the experimental FOI (Fig. 7), it appears that the behaviour of the cells cycled at temperatures of 25 °C and above are in line with LLI in combination with LAMdePE. While LLI is moving F1 towards higher voltages, LAMdePE pushes F1 towards lower voltages. Dubarry et all. [12] pointed out that F1 can be a good

indicator of the LAMdePE/LLI ratio. If F1 is not moving at all, the effect of LAMdePE and LLI are cancelling each other. The intensity decrease of F1 and F2 for the cells cycled at 15 °C and lower, in combination with a positive potential shift and an increase in F3, indicate a combination of LLI with LAMdeNE, pointing to Li plating. Although, the behaviour of F3 and the behaviour of the smaller peaks between F1 and F2 appears to not be in line with any simulated mode and might again point towards inhomogeneities, which are not included in the simulations.

4.1.5. Step V. ICA Comparison and Summary

In conclusion, we see that degradation and capacity loss do not always correlate. Even though the rate of capacity loss appeared to be very similar for cells cycled at an ambient temperature of 15 °C and 25 °C, as well as 5 °C and 35 °C, the degradation modes and mechanisms appear to be very different. Using ICA, the degradation of cells cycled at 25 °C and higher show similar degradation behaviour, as well as 15 °C and lower. In general, LLI appears to be the main degradation mechanism, accompanied by LAMdePE for cells cycled at 25 °C and higher. The cells cycled at lower temperatures indicate a large degree of inhomogeneities. Increased LLI at high temperatures could be due to an increased SEI growth rate at high temperatures [34], while at low temperatures it could be rather caused by Li plating.

4.2. 64 Ah Cell: Effect of Clamping

We analyzed the effect of clamping using the same 5-step procedure as was explained in detail in the previous section for the effect of ambient temperature. However, in the following, we will only present and point out the most important and interesting observations and conclusions.

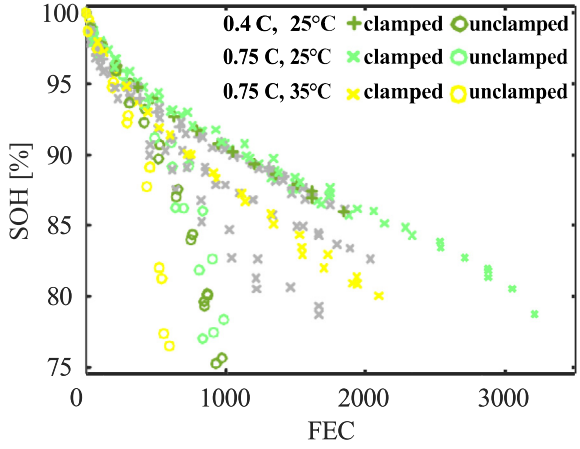

(a) SOH vs FEC

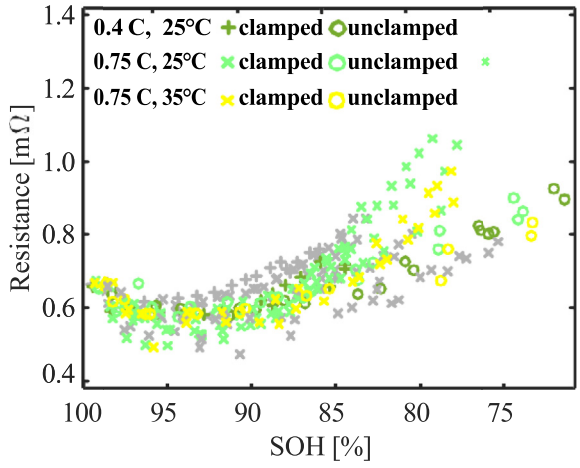

(b) 3min DC resistance at 50 %SOC during charge

Fig. 11. SOH versus FEC and DC resistance for the 64 Ah Cell, the effect of clamping during cycling.

4.2.1. Step I. Capacity and Resistance

Fig. 11 presents the SOH versus FEC and resistance versus SOH. Only cells that were cycled without mechanical clamping, and those cells with the exact same operating conditions but with mechanical clamping, are coloured. Clamped cells appear to have significantly better capacity retention compared to unclamped cells cycled at otherwise the same conditions. Comparing cells cycled at an ambient temperature of 25 °C with a 0.75 C charging and discharging rate, a SOH of 80 % is reached after about 900 FEC when not clamped, while around 3000 FEC are reached at the same conditions but clamped. The effect of clamping is significantly larger than the effect of ambient temperature. When only considering the unclamped cells, increasing the ambient temperature to 35 °C appears to have a similar accelerated ageing effect as observed for clamped cells. The resistance increase is lower at similar SOH for unclamped cells, indicating that the reduction in SOH is caused by other degradation modes.

4.2.2. Step II. Qualitative ICA

The difference in the IC curves between clamped cells compared to cells without clamping does not appear to be very significant. The full IC curves are therefore not presented but only the FOI analysis (Step III).

4.2.3. Step III. Feature ICA

Looking at the extracted FOI there are a few distinct differences. The potential shift of F3 appears to show the most significant difference between the cells cycled with and without MP (Fig. 7 E, grey circles). Initially, the cells cycled without clamping show a linear relationship between potential shift and SOH as clamped cells. Once the SOH is below about 90 %, the relationship becomes non-linear and the feature stops shifting much further. Interestingly this is around the same SOH at which the cells cycled at low ambient temperatures start deviating from the linear relationship as well. However, whereas the potential shift increases for the low-temperature cells, it stagnates for the unclamped cells. We also observe a little faster reduction of the intensity of F1 and a slightly slower reduction of the intensity of F2 compared to clamped cells. This difference becomes very clear when looking at the ratio of F1 intensity to F2 intensity in Fig. 12, which shows the distinctly different behaviour in how the ratio evolves for

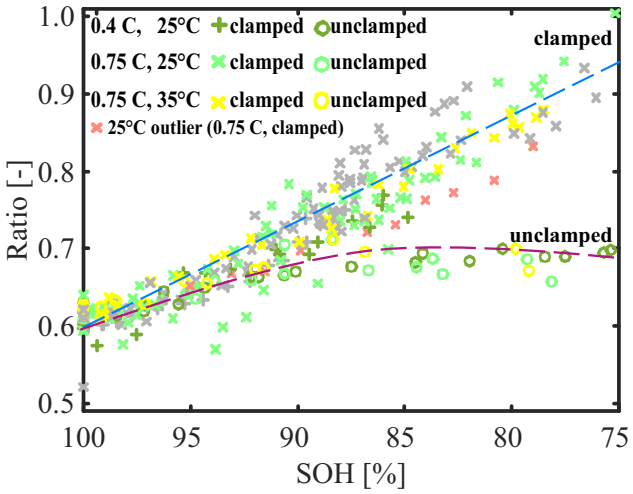

Fig. 12. Ratio of F1 intensity to F2 intensity, the effect of clamping during cycling.

the clamped cells versus unclamped cells. For clamped cells, this ratio is proportional to the SOH. F1 has an intensity of around 60 % of F2 at BOL and increases linearly with some differences in the slope. On the other hand, unclamped cells only follow a similar trend until a SOH of about 90 % is reached. With a further decrease in SOH, the ratio stays constant at around 70 %. The significantly different behaviour of the ratio for the unclamped cells results from the combination of both F1 losing more intensity with a reduction in capacity while the intensity of F2 faints less strongly compared to the clamped cells. The light red data points represent again the outlier of the cells cycled at ambient temperatures of 25°C where the clamping was replaced after around 300 FEC. Again, as observed especially for the potential of F3, the cell deviates from other cells cycled with the same conditions towards the cells without mechanical clamping.

4.2.4. Step IV. IC Simulation

Comparing the behaviour of the features with loss of capacity from the experimental data (Fig. 7) with the simulated data (Fig. 10), it appears that LLI is the main degradation mode, initially similar to the cells that were cycled with applied MP. After the initial capacity loss of about 10 %, especially the behaviour of F1 and F3 indicate that LAM becomes an important degradation mode. In addition, we recall again the clepsydra effect of LLI: LLI is observed first towards the end of the charge when Li is missing in the system (liquid missing in the clepsydra). LLI results in a loss in intensity of F2 first while F1 would still not be affected by missing Li, therefore the ratio of F1 intensity to F2 intensity increases. As the ratio stops increasing for unclamped cells at around 90 % SOH, it clearly shows how LLI is not the main degradation mode anymore.

4.2.5. Step V. Comparison and Summary

In summary, LLI appears to be the main degradation mechanism until the cell has lost about 10% capacity. After this, LAM is clearly impacting the IC curves. For graphite based cells, LAMdeNE and therefore a lowering of the LR results in plating and with this increasing the rate of LLI. This is in agreement with Dubarry [12] where this was explained by the LR larger than 1 compensating for the initial LAMdeNE. Unclamped cells already reach a SOH of 90 % after approximately 50 % of FEC compared to clamped cells with otherwise the same operating conditions. The rate of LLI appears to be significantly larger. Possible reasons could be volume changes leading to particle cracking and therefore increased formation of SEI and irreversible Li plating. Both are considered to benefit from adding pressure at low C rates (<0.8 C) e.g suppressing lithium dendrite formation [35,36]. This hypothesis is supported by the observed thickness changes of the cells due to degradation which were more significant for unclamped cells. The thickness of the cells increases linearly with the reduction in SOH. The thickness is increased between 25% to 30% at a SOH of 80%. More details are available in the *Supplementary Material*.

It appears that the faster capacity loss especially after the initial 10 % capacity loss for unclamped cells is due to additional LAM. Possible reasons here could be the particle cracking and isolation of particles [35,37], and trapped gas which prevents usage of parts of the active surface area [38].

Overall, simulation in combination with peak analysis allows observing differences that are more difficult to just see from the IC curve alone.

4.3. 31 Ah Cell: Method Transferability

To show how the method and simulation could be transferred to other cells and older data sets, we analyse the degradation of the *31 Ah Cell* with the same 5-step procedure as the *64 Ah Cell*. This provides an example of applying the method on other data sets. The *31 Ah Cell* is a NMC433/Graphite cell, which was cycled in relation to previous experiments. All degradation tests have been done without mechanical clamping.

4.3.1. I. Capacity and Resistance

Fig. 13 shows the capacity fade versus FEC and resistance versus SOH for the *31 Ah Cell* when cycled in the full SOC window. A change in ambient temperature appears to have a drastic effect on the capacity loss of the *31 Ah Cell*. The cell clearly has the longest cycle life at a moderate ambient temperature (25 °C), while the capacity is reduced significantly for an increased ambient temperature of 45 °C. The cell appears to fail right away at a low ambient temperature of 5 °C, resulting in a large gap in the data (that is used for ICA) down to 70 % SOH. A poor cycling performance at low temperatures and moderate to high C rates has often been shown to be due to Li plating on the negative electrode [39]. Interestingly, this was not observed for the *64 Ah Cell* which was cycled clamped, at the same temperature and at a slightly lower C rate. Applying mechanical pressure is discussed to reduce plating at moderate-high C rates (< 1C)[40,41]. The resistance (Fig. 13 b) increases most significantly for the cells cycled at high ambient temperatures. It increases the least for the low-temperature cells over the lifetime. This might be due to the low amount of duty cycling the cells at low temperatures managed to do before failing.

4.3.2. Step II. Qualitative ICA

The IC curves after an initial capacity loss of about 5 %, and towards the end-of-life (approximately 70 % SOH), are presented in Fig. 14. The IC curve of the *31 Ah Cell* looks similar to the IC curve of the *64 Ah Cell* (Fig. 6), but there are some differences. F1 has a lower

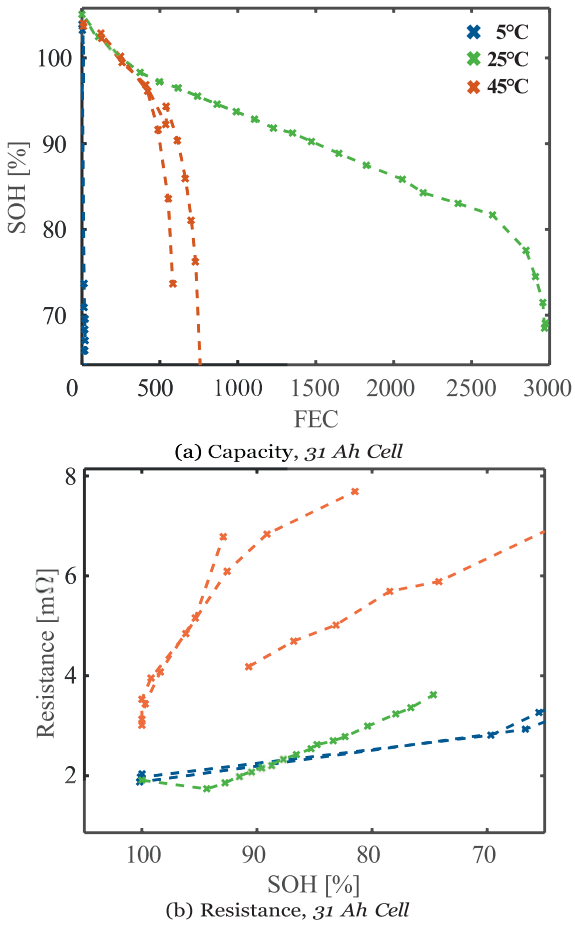

Fig. 13. Capacity and Resistance of the *31 Ah Cell*, full SOC window, no clamping, different ambient temperatures.

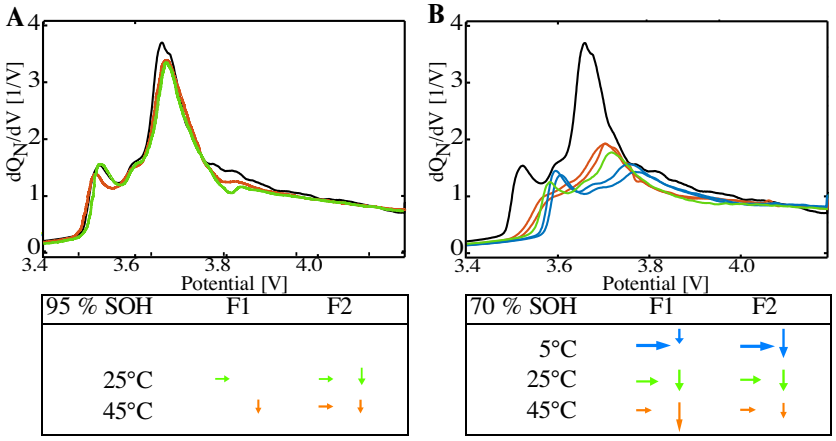

Fig. 14. IC curves at 95±1 % SOH, and 70±1 %SOH for the *31 Ah Cell*, cycled at different ambient temperatures.

intensity for the *31 Ah Cell*, and both F1 and F2 are at slightly higher potentials compared to the *64 Ah Cell*. This could be caused partly by both the higher C-rate used for the *31 Ah Cell* (C/10), as well as the higher internal resistance. A minimum at high potentials (F3) is also not visible for the *31 Ah Cell* at BOL. Therefore, we only focus on F1 and F2 in the following.

At 95 % SOH (Fig. 14 A), both FOI shift to higher potentials for the cell cycled at room temperature. For the high-temperature cell, the start of F1 stays at the same potential while F2 shifts to higher potentials. Both features drop in intensity for the high-temperature cells while only F2 drops in intensity for the room-temperature cell. At approximately 70 % SOH (Fig. 14 B), both FOI have shifted to higher potentials. The largest shift was seen for the low temperature, whereas the high-temperature cells show the smallest shift. We recall that the resistance increased for all cells but the correlation with temperature was inverse (i.e. largest resistance increase for high temperatures). For high temperatures, both FOIs become less distinguishable as two separate features. Both features also lose intensity. F1 drops in intensity most extremely for high-temperature, whereas F2 drops in intensity most extremely for cold temperatures. The observations described are summarized in the tables below the graphs. As the limited availability of degradation data in the old *31 Ah Cell* data set, 95 % (only 25 °C and 45 °C) and 70 % SOH were selected but do not allow for a for direct comparison with the *64 Ah cell* at this level. However, the comparison of FOIs allows for comparing the trends between the data sets even though there is no data available that allow for a direct comparison at different SOH.

4.3.3. Step III. Feature ICA

Fig. 15 presents the potential shift and intensity of F1 and F2 of the *31 Ah Cell*. The potential change of F1 appears to be proportional to the SOH, similarily to the *64 Ah cells* cycled at low temperatures. Although, for the high-temperature cell an initial shift to lower potential is observed, which is in agreement with the *64 Ah Cell*. The intensity of F1 (Fig. 15 B) is decreasing linear to the loss of capacity for the cells cycled at room temperature, while cells cycled at low (5°C) and high (45°C) temperatures, vary from this. The intensity of the high-temperature cells drops even though the SOH initially does not decrease (compare to Fig. 13a). After this initial onset, it starts decreasing linearly with a reduction in SOH, with a similar slope as the cells cycled at room-temperature (25°C). The potential shift of F1 (Fig. 15 A) to lower potentials appears very scattered and the intensity (Fig. 15 B) shows such a significant drop when plotted versus SOH. The F1 intensity of the low-temperature behaves similarly to the room-temperature cell for the initial capacity loss of up to 5 %. We recall that the low-temperature cells showed a very fast and drastic drop after the initial 5 % of capacity loss. The intensity of F1 does not change as drastically and is still larger than the room-temperature cells at a similar SOH. This behaviour of F1 intensity is the opposite of what was observed for the *64 Ah Cell*, where the low-temperature cells dropped faster in F1 intensity than the cells at 25°C and higher. However, we recollect that for the *64 Ah Cell* the low-temperature cell had better capacity retention than the high-temperature cell.

The potential change of F2 (Fig. 15 C) is proportional to the SOH for cells cycled at 25°C and higher. The shift to higher potentials is more extreme for the cells cycled at low-temperatures. This observation is in agreement with what was observed for the *64 Ah Cell*. Comparing this with the OR (Fig. 13b), we notice that this behaviour can not only be explained by an increase in OR as this would result in a potential shift that is most extreme for the high-temperature cells and the lowest for the low-temperature cells. (This is confirmed when calculating the IR drop from the resistance.) The intensity of F2 decreases linearly with capacity loss independent of the temperature the cell has been cycled at. This is not fully in agreement with the *64 Ah Cell*, where the intensity decreased more or less linearly except for a more rapid loss of intensity for low-temperature cells below a SOH of approximately 92.5 %.

4.3.4. Step IV. IC Simulation

The degradation map and FOIs from the simulations based on the half-cell data of the *64 Ah Cell* are used, as no half-cell data of the *31 Ah Cell* was available. Although conclusions and comparisons have to be done more carefully, using simulated degradation maps from similar cell compositions if no-half cell data is available has also been suggested by Dubarry et al. [12]. The FOI versus SOH map generated for *64 Ah Cell* was used for the *31 Ah Cell* and appears to be fair as the negative electrode and positive electrode materials are very similar.

Step IVi. IC Simulation: Qualitative comparison. Comparing the experimental IC curves (Fig. 14) with the degradation map (Fig. 9), again helps to discuss degradation modes. For low-temperature cells, it appears that the intensity of F2 is decreasing more extremely than F1, indicating a stronger influence of LLI. As discussed earlier, the LLI has a large effect on the FOI closer to the end of the charge. The drastic capacity loss due to LLI could be due to large amounts of irreversible Li plating. For the high-temperature cells, a shift of F1 to lower potentials was observed initially, even though the resistance is increasing. After this, the intensity of F1 starts to decrease and the peak shifts to higher potentials before nearly vanishing, while F2 is decreasing less extremely. This behaviour is in agreement with what appears to be characteristic of LAM, as the chemical reaction will occur sooner.

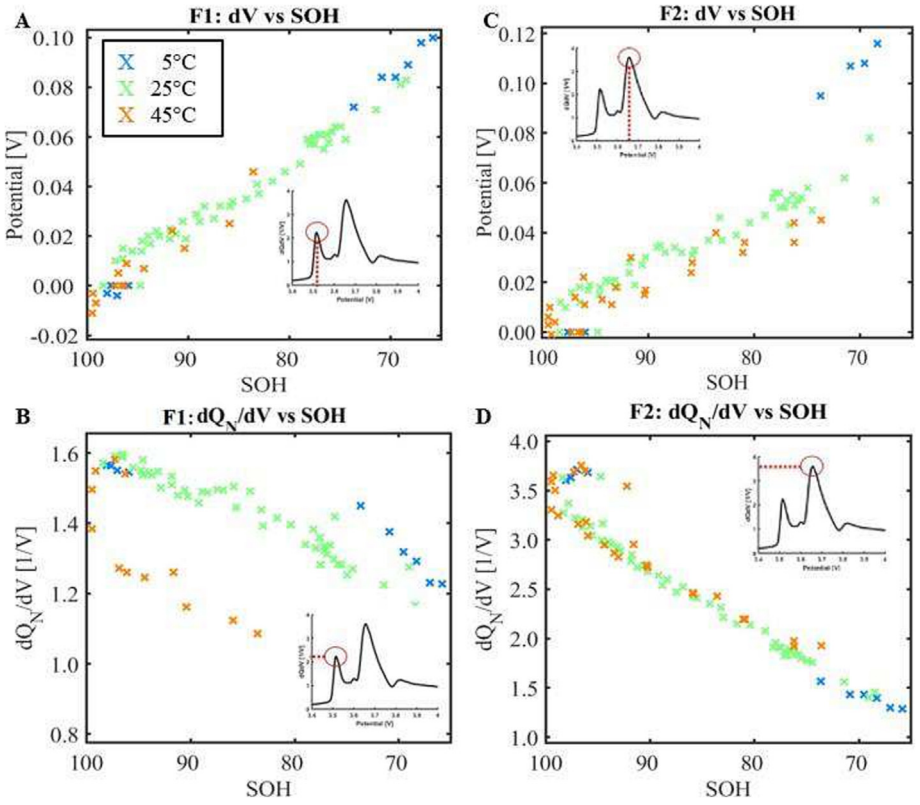

Fig. 15. Intensity and potential shift of F1 and F2 versus SOH for the *31 Ah Cell* for different ambient temperatures, 1 C charging and discharging rate, no mechanical clamping.

Step IVii. IC Simulation: FOI Comparing the FOIs of the experimental data (Fig. 15) with the FOI of the simulation (Fig. 10), we confirm that LLI is the main degradation mode at low-temperature. This explains the more extreme loss in intensity of F2 compared to F1 and a shift to higher potentials. However, for the high-temperature cells, the extreme drop in intensity of F1 (compare Fig. 15 B and 10) without any initial loss in capacity, (compare Fig. 13a and 9), as well as the initial shift to lower potentials (compare Fig. 15 A and 10), are well aligned with LAM both at the negative and positive electrode.

4.3.5. Step V. Comparison and Summary

In summary, it appears that LLI is the main degradation mode for all cells. It appears to be responsible for the poor cycling performance for the cells cycled at 5°C, while LAM also appears to be important for the cells cycled at 45°C. The LLI at 5°C points to very fast and irreversible plating.

4.4. Overall Summary and Discussion

Comparing the conducted ICA for the *64 Ah Cells* and the *31 Ah Cells*, both cells showed the best capacity retention at room temperature, which was decreased at both high and low temperatures. However, for the *31 Ah Cell* the capacity dropped below 80 % already after a few duty cycles at 5°C, while for the *64 Ah Cell* showed a similar cycling life to cells cycled at 35°C.

The internal resistance behaved very different in the two types of cells. While for the *31 Ah Cell* the resistance increased the most for high temperature, it increased the fastest for low and room temperature for the *64 Ah Cell*. The latter showed the slowest increase at high temperatures.

The potential shift of F1 was proportional to the SOH for both cells, after an initial shift to lower potentials for cells cycled at high-temperatures. However, the intensity of F1 showed opposite trends for both cells. It dropped the fastest for high temperatures and the slowest for low temperature for *31 Ah Cell* and behaved the other way around for the *64 Ah Cell*.

The potential shift of F2 showed similar trends for both cells, being more extreme at low temperatures. The intensity decreased linearly for both cells, but deviated from this for the low-temperature *64 Ah Cell* cells below a SOH of 92 %. The initial negative potential shift of F1 for both cells at high-temperature indicated the LAMdePE, as it is the only mode that results in a negative potential shift of F1. The significant drop in F1 intensity indicates that for the high-temperature *31 Ah Cell* this is accompanied by LAMdeNE. For low temperature *31 Ah Cells*, the small loss in intensity of F1 compared to the strong loss in F2 intensity strongly suggests that LLI is the main DM. For *64 Ah Cell*, on the other hand, F1 does not loose intensity as significantly, and especially not in comparison with F2. This suggests that LLI is not the prevalent DM alone in this case. Extreme plating is not observed, which could be due to the clamping. However, it is not possible to conclude as it is two different cells, and the *64 Ah cell* cell was cycled without clamping at 5°C.

5. Conclusion

Simulations in combination with peak analysis allows observing differences that are difficult to identify from the IC curves alone.

We observe that degradation and capacity loss do not always correlate. Despite the rate of capacity loss appeared to be very similar for clamped cells cycled at 15 °C and 25 °C, as well as 5 °C and 35 °C for the *64 Ah Cell*, the degradation modes and mechanisms appear to be very different. It appears, that no single FOI is a good direct indicator of SOH across all ambient temperatures. Validation data is needed across a wider temperature range when FOI are to be used for SOH

estimation. Using ICA, the degradation of cells cycled at 25 °C and higher, as well as 15 °C and lower, show similar degradation behaviour. In general, LLI appears to be the main degradation mechanism, especially for cells cycled at higher temperatures, while the cells cycled at lower temperatures indicate a large degree of inhomogeneous degradation within the single cells.

The *64 Ah Cell* without mechanical clamping reached a SOH of 90 % after approximately 50 % of FEC compared to clamped cells, with otherwise the same operating conditions. It appeared that the faster capacity loss, especially after the initial 10 % capacity loss for cells without any applied MP, was due to additional LAM.

The *31 Ah Cell* without mechanical clamping showed a very poor cycling performance for cells cycled at low temperatures. ICA revealed LLI to be responsible, pointing to a very fast and irreversible plating.

With a suitable FOI versus SOH map, the FOI appears to enable a simple approach of identifying if cells have been pressurized during the use phase and narrowing down the temperature range a cell has been cycled at. A possible option for applying this process is identifying cells with unknown cycling histories suitable for second-life applications.

Declaration of Competing Interest

The authors declare that they have no known competing financial interests or personal relationships that could have appeared to influence the work reported in this paper.

Acknowledgement

Authors would like to thank Matthieu Dubarry and the University of Hawai'i at Mānoa for sharing the 'alawa battery emulation toolbox. The authors would like to acknowledge the Research Council of Norway and partner companies of the BATTMAriNe project for finacial supportunding, Grant No. 281005 The authors would like to acknowledge the Research Council of Norway and the KeyTech-NeVe-ChiNo project for financial support, Grant No. 304213. The authors would like to acknowledge ENERSENSE funded by NTNU for financial support, Grant No. 68024013.

References

[1] O. Burheim, Engineering Energy Storage, Academic Press, 2017.
[2] S. Jenu, I. Deviatkin, A. Hentunen, M. Myllysilta, S. Viik, M. Pihlatie, Reducing the climate change impacts of lithium-ion batteries by their cautious management through integration of stress factors and life cycle assessment, Journal of Energy Storage 27 (2020) 101023.
[3] M. Dubarry, C. Truchot, B.Y. Liaw, Synthesize battery degradation modes via a diagnostic and prognostic model, Journal of power sources 219 (2012) 204–216.
[4] M. Dubarry, N. Qin, P. Brooker, Calendar aging of commercial li-ion cells of different chemistries–a review, Current Opinion in Electrochemistry 9 (2018) 106–113.
[5] F. Richter, S. Kjelstrup, P.J. Vie, O.S. Burheim, Thermal conductivity and internal temperature profiles of li-ion secondary batteries, Journal of Power Sources 359 (2017) 592–600, https://doi.org/10.1016/j.jpowsour.2017.05.045.
[6] E. Sarasketa-Zabala, I. Gandiaga, L.M. Rodriguez-Martinez, I. Villarreal, Calendar ageing analysis of a lifepo 4/graphite cell with dynamic model validations: Towards realistic lifetime predictions, Journal of Power Sources 272 (2014) 45–57.
[7] E. Sarasketa-Zabala, I. Gandiaga, E. Martinez-Laserna, L.M. Rodriguez-Martinez, I. Villarreal, Cycle ageing analysis of a lifepo4/graphite cell with dynamic model validations: Towards realistic lifetime predictions, Journal of Power Sources 275 (2015) 573–587.
[8] J. Wang, P. Liu, J. Hicks-Garner, E. Sherman, S. Soukiazian, M. Verbrugge, H. Tataria, J. Musser, P. Finamore, Cycle-life model for graphite-lifepo4 cells, Journal of Power Sources 196 (8) (2011) 3942–3948.
[9] A. Barai, K. Uddin, M. Dubarry, L. Somerville, A. McGordon, P. Jennings, I. Bloom, A comparison of methodologies for the non-invasive characterisation of commercial li-ion cells, Progress in Energy and Combustion Science 72 (2019) 1–31.
[10] F. Zheng, M. Kotobuki, S. Song, M.O. Lai, L. Lu, Review on solid electrolytes for all-solid-state lithium-ion batteries, Journal of Power Sources 389 (2018) 198–213.
[11] R.A. Huggins, Energy storage fundamentals materials and applications, 2nd Edition., Springer, 2016.
[12] M. Dubarry, D. Anseán, Best practices for incremental capacity analysis, Frontiers in Energy Research 10..
[13] J. Tian, R. Xiong, Q. Yu, Fractional-Order Model-Based Incremental Capacity Analysis for Degradation State Recognition of Lithium-Ion Batteries, IEEE Transactions on Industrial Electronics 66 (2) (2019) 1576–1584, https://doi.org/10.1109/TIE.2018.2798606.
[14] X. Li, C. Yuan, X. Li, Z. Wang, State of health estimation for Li-Ion battery using incremental capacity analysis and Gaussian process regression, Energy 190 (2020), https://doi.org/10.1016/j.energy.2019.116467 116467.
[15] J. Zhu, M.S. Dewi Darma, M. Knapp, D.R. Sørensen, M. Heere, Q. Fang, X. Wang, H. Dai, L. Mereacre, A. Senyshyn, X. Wei, H. Ehrenberg, Investigation of lithium-ion battery degradation mechanisms by combining differential voltage analysis and alternating current impedance, Journal of Power Sources 448 (2020) (November 2019) 28–30, https://doi.org/10.1016/j.jpowsour.2019.227575.
[16] M. Dubarry, M. Berecibar, A. Devie, D. Anseán, N. Omar, I. Villarreal, State of health battery estimator enabling degradation diagnosis: Model and algorithm description, Journal of Power Sources 360 (2017) 59–69, https://doi.org/10.1016/j.jpowsour.2017.05.121.
[17] L. Zheng, J. Zhu, D.D.C. Lu, G. Wang, T. He, Incremental capacity analysis and differential voltage analysis based state of charge and capacity estimation for lithium-ion batteries, Energy 150 (2018) 759–769, https://doi.org/10.1016/j.energy.2018.03.023.
[18] D.I. Stroe, E. Schaltz, Lithium-Ion Battery State-of-Health Estimation Using the Incremental Capacity Analysis Technique, IEEE Transactions on Industry Applications 56 (1) (2020) 678–685, https://doi.org/10.1109/TIA.2019.2955396.
[19] M. Berecibar, M. Dubarry, N. Omar, I. Villarreal, J. Van Mierlo, Degradation mechanism detection for nmc batteries based on incremental capacity curves, World Electric Vehicle Journal 8 (2) (2016) 350–361.
[20] C. Pastor-Fernández, K. Uddin, G.H. Chouchelamane, W.D. Widanage, J. Marco, A Comparison between Electrochemical Impedance Spectroscopy and Incremental Capacity-Differential Voltage as Li-ion Diagnostic Techniques to Identify and Quantify the Effects of Degradation Modes within Battery Management Systems, Journal of Power Sources 360 (2017) 301–318, https://doi.org/10.1016/j.jpowsour.2017.03.042.
[21] K.A. Severson, P.M. Attia, N. Jin, N. Perkins, B. Jiang, Z. Yang, M.H. Chen, M. Aykol, P.K. Herring, D. Fraggedakis, M.Z. Bazant, S.J. Harris, W.C. Chueh, R.D. Braatz, Data-driven prediction of battery cycle life before capacity degradation, Nature Energy 4 (5) (2019) 383–391, https://doi.org/10.1038/s41560-019-0356-8.
[22] S. Kim, A. Raj, B. Li, E.J. Dufek, C.C. Dickerson, H.Y. Huang, B. Liaw, G.M. Pawar, Correlation of electrochemical and mechanical responses: Differential analysis of rechargeable lithium metal cells, Journal of Power Sources 463 (January) (2020), https://doi.org/10.1016/j.jpowsour.2020.228180 228180.
[23] A. Fly, R. Chen, Rate dependency of incremental capacity analysis (dQ/dV) as a diagnostic tool for lithium-ion batteries, Journal of Energy Storage 29 (March) (2020), https://doi.org/10.1016/j.est.2020.101329 101329.
[24] K.S. Mayilvahanan, K.J. Takeuchi, E.S. Takeuchi, A.C. Marschilok, A.C. West, Supervised Learning of Synthetic Big Data for Li-Ion Battery Degradation Diagnosis, Batteries and Supercaps 5 (1). doi:10.1002/batt.202100166..
[25] X. Li, Z. Wang, L. Zhang, C. Zou, D.D. Dorrell, State-of-health estimation for Li-ion batteries by combing the incremental capacity analysis method with grey relational analysis, Journal of Power Sources 410–411 (November 2018) (2019) 106–114. doi:10.1016/j.jpowsour.2018.10.069. URL: doi: 10.1016/j.jpowsour.2018.10.069..
[26] L. Zheng, J. Zhu, D.D.-C. Lu, G. Wang, T. He, Incremental capacity analysis and differential voltage analysis based state of charge and capacity estimation for lithium-ion batteries, Energy 150 (2018) 759–769.
[27] X. Bian, Z. Wei, W. Li, J. Pou, D.U. Sauer, L. Liu, State-of-health estimation of lithium-ion batteries by fusing an open circuit voltage model and incremental capacity analysis, IEEE Transactions on Power Electronics 37 (2) (2021) 2226–2236.
[28] C. She, Z. Wang, F. Sun, P. Liu, L. Zhang, Battery aging assessment for real-world electric buses based on incremental capacity analysis and radial basis function neural network, IEEE Transactions on Industrial Informatics 16 (5) (2019) 3345–3354.
[29] A. Fly, R. Chen, Rate dependency of incremental capacity analysis (dq/dv) as a diagnostic tool for lithium-ion batteries, Journal of Energy Storage 29 (2020) 101329.
[30] M. Dubarry, G. Baure, A. Devie, Durability and Reliability of EV Batteries under Electric Utility Grid Operations: Path Dependence of Battery Degradation, Journal of The Electrochemical Society 165 (5) (2018) A773–A783, https://doi.org/10.1149/2.0421805jes.
[31] M. Dubarry, D. Beck, Analysis of synthetic voltage vs. capacity datasets for big data li-ion diagnosis and prognosis, Energies 14 (9) (2021) 2371.
[32] L. Spitthoff, P.R. Shearing, O.S. Burheim, Temperature, ageing and thermal management of lithium-ion batteries, Energies 14 (5) (2021) 1248.
[33] T. Waldmann, M. Wilka, M. Kasper, M. Fleischhammer, M. Wohlfahrt-Mehrens, Temperature dependent ageing mechanisms in lithium-ion batteries – a post-mortem study, Journal of Power Sources 262 (2014) 129–135.
[34] P.M. Attia, S. Das, S.J. Harris, M.Z. Bazant, W.C. Chueh, Electrochemical kinetics of sei growth on carbon black: Part i, experiments, Journal of The Electrochemical Society 166 (4) (2019) E97.
[35] C. Niu, H. Lee, S. Chen, Q. Li, J. Du, W. Xu, J.-G. Zhang, M.S. Whittingham, J. Xiao, J. Liu, High-energy lithium metal pouch cells with limited anode swelling and long stable cycles, Nature Energy 4 (7) (2019) 551–559.

[36] S. Müller, P. Pietsch, B.-E. Brandt, P. Baade, V. de Andrade, F. de Carlo, V. Wood, Quantification and modeling of mechanical degradation in lithium-ion batteries based on nanoscale imaging, Nature communications (2018) 2340.
[37] F.P. McGrogan, S.N. Raja, Y.-M. Chiang, K.J. Van Vliet, Electrochemomechanical fatigue: decoupling mechanisms of fracture-induced performance degradation in lixmn2o4, Journal of The Electrochemical Society 165 (11) (2018) A2458.
[38] R. Weber, M. Genovese, A. Louli, S. Hames, C. Martin, I.G. Hill, J. Dahn, Long cycle life and dendrite-free lithium morphology in anode-free lithium pouch cells enabled by a dual-salt liquid electrolyte, Nature Energy 4 (8) (2019) 683–689.
[39] W. Cai, C. Yan, Y.-X. Yao, L. Xu, X.-R. Chen, J.-Q. Huang, Q. Zhang, The boundary of lithium plating in graphite electrode for safe lithium-ion batteries, Angewandte Chemie International Edition 60 (23) (2021) 13007–13012.
[40] V. Müller, R.-G. Scurtu, M. Memm, M.A. Danzer, M. Wohlfahrt-Mehrens, Study of the influence of mechanical pressure on the performance and aging of lithium-ion battery cells, Journal of Power Sources 440 (2019) 227148.
[41] X. Zhang, Q.J. Wang, K.L. Harrison, K. Jungjohann, B.L. Boyce, S.A. Roberts, P.M. Attia, S.J. Harris, Rethinking how external pressure can suppress dendrites in lithium metal batteries, Journal of The Electrochemical Society 166 (15) (2019) A3639.